Available online at www.sciencedirect.com
ScienceDirect
Journal of Power Sources 160 (2006) 232–245
JOURNAL OF POWER SOURCES
www.elsevier.com/locate/jpowsour

Effects of parameter uncertainty on the performance variability of proton exchange membrane (PEM) fuel cells

A. Mawardi, R. Pitchumani *

Advanced Materials and Technologies Laboratory, Department of Mechanical Engineering, University of Connecticut, Storrs, CT 06269-3139, United States

Received 4 December 2005; received in revised form 3 January 2006; accepted 5 January 2006
Available online 17 February 2006

Abstract

Operation of fuel cells is subject to inherent uncertainty in various material and operating parameters, which causes performance variability and impacts the reliability of the cells. Analysis of the interactive effects of parameter uncertainty on the fuel cell performance is imperative in a robust design endeavor. To this end, a methodology for simulation of fuel cell operation under uncertainty is presented by considering a one-dimensional nonisothermal description of the governing physical phenomena. A sampling-based stochastic model is developed, and parametric analysis is presented to elucidate the effects of uncertainty in several operating parameters on the variability of power density of the fuel cell. Robust design maps are derived from the analysis which provide for selection of cell temperature and anode and cathode pressures as functions of the input parameter uncertainty and target maximum acceptable variability in the power density.
© 2006 Elsevier B.V. All rights reserved.

Keywords: Proton exchange membrane (PEM) fuel cell; Stochastic analysis; Design under uncertainty

1. Introduction

Power sources consisting of proton exchange membrane (PEM) fuel cells offer the advantages of low operating temperature and pressure, quick start-up, and pollution-free operation [1]. The overall cell performance is governed by the critical issues of water and thermal management [2–7]. Extensive studies on modeling and computer simulation of PEM fuel cells have been developed towards improved water and thermal management through better understanding the transport and electrochemical processes. Bernardi and Verbrugge [8,9], Springer et al. [10,11], Baschuk and Li [12], and Rowe and Li [13] developed one-dimensional models for steady state operation of fuel cells, assuming perfect membrane hydration. Amphlett et al. [14,15] studied the transient response of a fuel cell stack by performing a global heat and mass balance analysis, and the details of electrochemical phenomena inside the cell were ignored. Two-dimensional modeling of transport phenomena in PEM fuel cells was presented by Gurau et al. [16], Um et al. [17], Wang et al. [18], You and Liu [19] and You [20], where two-phase flows in the fuel cell systems were also discussed. Mishra et al. [21] reported theoretical and experimental study on the effects of different gas diffusion layer materials and contact pressure on the electrical contact resistance. A methodology for model-based design based on a one-dimensional nonisothermal model was presented by Mishra et al. [22], in which the optimum operating and design parameters were identified using a comprehensive parametric analysis on the various physical and electrochemical phenomena. Mawardi et al. [23] extended this analysis to provide an optimization framework to derive more general optimum solutions.

The application of cell level models to predicting the fuel cell performance is based on the assumption that the parameters representing the physical and electrochemical phenomena, and the material properties of the fuel cell are deterministic. It must be realized that significant uncertainty is inherent in such parameters [24,25], arising from sources such as operating parameter fluctuations, inaccuracies in process control, empirical determination of the electrochemical model parameters, and environmental uncertainties. Operating parameters such as cell temperature, anode and cathode pressures, relative humidity, reactants stoichiometry, and dry gas mole fractions

* Corresponding author. Tel.: +1 860 486 2090; fax: +1 860 486 5088.
E-mail address: r.pitchumani@uconn.edu (R. Pitchumani).

0378-7753/$ – see front matter © 2006 Elsevier B.V. All rights reserved.
doi:10.1016/j.jpowsour.2006.01.017

Nomenclature

a	active area per unit volume ($cm^2\ cm^{-3}$)
c_i	molar concentration of species i ($mol\ cm^{-3}$)
$c_{p,i}$	molar heat capacity at constant pressure for species i ($J\ mol^{-1}\ K$)
F	Faraday constant 96487 ($C\ mol^{-1}$)
h_{vap}	mass enthalpy of vaporization ($J\ g^{-1}$)
i_0	exchange current density ($A\ cm^{-2}$)
i_m	catalyst layer membrane phase current density ($A\ cm^{-2}$)
I	operating current density ($A\ cm^{-2}$)
k	thermal conductivity ($J\ cm^{-1}\ K$)
k_p	hydraulic permeability (cm^2)
N_i	molar flux of species i ($mol\ cm^{-2}\ s$)
p	pressure (atm)
P_d	power density ($W\ cm^{-2}$)
R	universal gas constant 8.314 ($J\ mol^{-1}\ K$)
RH	relative humidity
ΔS	entropy change ($J\ g^{-1}\ K$)
T	cell temperature (K)
W_i	molar mass of species i ($cm\ s^{-1}$)
x	position co-ordinate along the cell thickness
x_i	mole fraction of species i

Greek symbols

α_a	transfer coefficient for anodic reaction
α_c	transfer coefficient for cathodic reaction
δ	membrane expansion coefficient
ϵ_w^{mem}	volume fraction of water in the membrane
ζ	stoichiometry
η_d	electro-osmotic drag coefficient
θ_i	fractional coverage of species i
κ	proton conductivity of the membrane ($W\ cm^{-1}\ K$)
λ	membrane hydration coefficient (moles of water/moles charge site)
μ_j	mean value of parameter j
μ_v	viscosity ($g\ cm^{-1}\ s$)
ξ	input parameter under uncertainty
σ_c	electrical conductivity of species ($\Omega\ cm^{-1}$)
σ_i	standard deviation of parameter j
Φ_m	membrane phase potential (V)
Φ_s	solid phase potential (V)
ω_i	mass source for species i ($g\ cm^{-1}$)

Subscripts

a	anode
c	cathode
cat	catalyst phase
crit	critical
el	electrode phase
l	liquid
max	maximum value
ref	reference

Superscripts

*	optimum value
i	boundary i
eff	effective

are subject to control fluctuations and thus may be considered uncertain. The empirical modeling of the electrochemical phenomena may render parameters such as the transfer coefficients in the Butler–Volmer equations, also to be uncertain. The interactive effects of the uncertainty in these parameters affect both the transport and electrochemical phenomena in all regions of the fuel cell, and must be understood.

A mathematical framework incorporating the interactive effects of parameter uncertainty on the performance of the fuel cell is necessary for a realistic, physics-based simulation and robust design. Simulations under uncertainty using the framework can, in turn, be used to identify the operating conditions that maximize the cell performance with minimum variability. To this end, a stochastic modeling framework is developed and illustrated by considering a one-dimensional, single-phase nonisothermal description of a PEM fuel cell operating on reformate feed. The stochastic modeling approach involves quantifying the uncertainty in the input parameters in the form of appropriate distribution functions, and propagating the uncertainty through a deterministic model to construct the output variability distributions [26,27]. The output distributions are, in turn, used to obtain reliability or robustness measures.

In the present implementation, the fuel cell material and operating parameters with uncertainty are represented as Gaussian probability distributions which are quantified in terms of the mean and the variance values. A sampling method is used to generate combinations of the input parameters (samples) from their respective distributions, and a one-dimensional nonisothermal model is used to simulate the fuel cell operation for each sample. The results of the simulations are used to construct probability distributions of the power density. The output distributions, in turn, provide for extracting the variability information needed in a robust design endeavor. Parametric analysis is performed to elucidate the effects of uncertainty in the operating and design parameters on the power density distribution for several values of the fuel cell temperature and pressures on the anode and cathode. It should be noted that, although the focus of the paper is on the PEM fuel cell, the stochastic analysis methodology presented herein is readily applicable to other types of fuel cell.

The paper is organized as follows: a deterministic PEM fuel cell model which forms the basis of the stochastic modeling is reviewed in Section 2, followed by a description of the sampling-based stochastic modeling framework in Section 3. Section 4 discusses the results of the stochastic analysis and the parametric studies leading to identification of robust operating maps.

2. Mathematical model of a PEM fuel cell

A comprehensive physical model for the transport and electrochemical phenomena presented by Mishra et al. [22] is used to simulate the performance of a PEM fuel cell operating on reformate feed. The model considers a typical PEM fuel cell, where a polymer membrane is placed between an anode and a cathode electrode to form a membrane-electrode-assembly (MEA). Two bipolar plates housing the flow channel are used to clamp the MEA, as shown in Fig. 1. Thin catalyst layers exist between each of electrodes and the membrane, referred to as the anode and cathode catalyst layer, respectively. The cell is considered to be operating at steady state, and since the primary aim of the study is to present a framework for stochastic analysis of fuel cells using physics-based models, the discussion is limited to a one-dimensional modeling in the direction along the cell thickness. The modeling further neglects two-phase flow effects, but these effects may be readily incorporated using approaches such as in Refs. [28–30]. The modeling includes the effects of carbon monoxide (CO) poisoning of the catalysts, as is prevalent in fuel cells operating on a reformate feed. The governing equations for the electrode, catalyst and membrane regions follow those given in Ref. [22] and are briefly reviewed in the subsections below.

2.1. Electrodes

Fuel cell electrodes are typically made of porous carbon paper or cloth, which serves to transfer the reactant species and to conduct electrical current. The mathematical model is obtained by considering the conservation of the species and energy. Following the development by Rowe and Li [13], the governing equations may be written as

$$\text{species}: \quad \frac{\mathrm{d}N_i}{\mathrm{d}x} = \frac{\omega_i}{W_i} \tag{1}$$

$$\text{energy}: \quad -k^{\text{eff}}\frac{\mathrm{d}^2T}{\mathrm{d}x^2} + \left[\sum_i N_i W_i c_{\mathrm{p},i} + N_{\mathrm{l}} W_3 c_{\mathrm{p,l}}\right]\frac{\mathrm{d}T}{\mathrm{d}x} + h_{\text{vap}}\omega_3 - \frac{I^2}{\sigma_{\mathrm{c}}^{\text{eff}}} = 0 \tag{2}$$

where the subscript $i = 1,\ldots,3$ denotes the ideal gas species i, N_i the molar flux in the x-direction in Fig. 1, ω_i the mass source term, W_i the molecular weight, k^{eff} the effective thermal conductivity, T the temperature, $c_{\mathrm{p},i}$ the specific heat at constant pressure, N_{l} the molar flux of liquid water, h_{vap} the enthalpy of vaporization for water, I the current density, $\sigma_{\mathrm{c}}^{\text{eff}}$, the effective electrical conductivity, and the summation $\sum_i$ is performed with respect to all the gas species in the mixture.

In this study, the feed streams are considered to be reformate fuel at the anode side and humidified air at the cathode side. Hence, the gas species i, $i = 1,\ldots,3$, are defined as $1 = O_2$, $2 = N_2$, $3 = H_2O(g)$ (i.e., water vapor) for the cathode electrode and $1 = H_2$, $2 = CO_2$, $3 = H_2O(g)$, and $4 = CO$ for the anode electrode. Since no electrochemical reaction occurs in the electrode regions, the mass source term ω_i is nonzero only for the water vapor species $i = 3$. To solve the water vapor flux N_3, the mass source term ω_3 (corresponding to the vaporization/condensation of the water species) is determined in terms of the temperature and species concentration x_3, which, in turn, is determined by the Stefan–Maxwell equation [13]. Furthermore, the electrical potential in the electrode solid, Φ_{s}, is calculated by Ohm's law, and the unknowns in the electrode regions are T, N_3, x_3, and Φ_{s}.

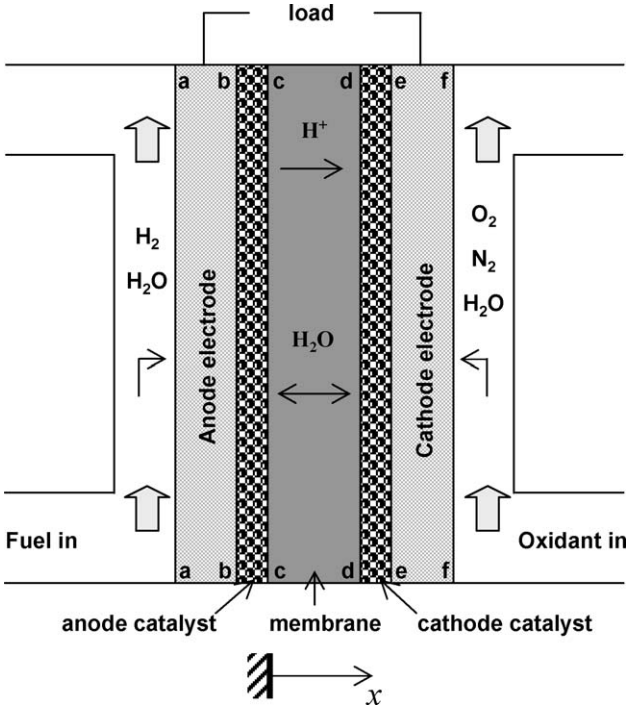

Fig. 1. Schematic illustration of a proton exchange membrane (PEM) fuel cell.

2.2. Catalyst layers

Catalyst layers are considered to be a mixture of membrane, platinum catalyst (solid), and void space in this study. Electrochemical reactions in the catalyst regions are coupled with the transport of mass and energy, resulting in a potential gradient across the cell. The CO and H_2 molecules in the fuel compete with each other for the vacant catalyst sites, and high concentration of CO may prevent the electrochemical reaction of the hydrogen molecules, leading to the so-called CO poisoning effect.

In this subsection, the subscript notation for the species involved in the anode catalyst layer is $1 = H_2$, $2 = H^+$, $3 = H_2O(l)$, $4 = CO$, $5 = CO_2$, and that for the cathode catalyst layer is $1 = O_2$, $2 = H^+$, $3 = H_2O(l)$. The governing equations for the various electrochemical and transport processes are derived by the application of conservation laws for the species and energy, along with the Butler–Volmer equation for the electrochemical reactions, the Nernst–Planck equation for the flux of aqueous species in the membrane, and the Ohm's law for electron transfer in the solid.

The conservation equations of species and energy in the anode catalyst layer account for the electrochemical reactions of CO and H_2 as follows:

$$\text{species } H_2: \quad \frac{dN_1}{dx} = -\frac{j_1(x)}{2F} \tag{3}$$

$$\text{species } H^+: \quad F\frac{dN_2}{dx} = \frac{di_m}{dx} = j_1(x) + j_4(x) \tag{4}$$

$$\text{species } H_2O(l): \quad \frac{dN_3}{dx} = -\frac{j_4(x)}{2F} \tag{5}$$

$$\text{species CO}: \quad \frac{dN_4}{dx} = -\frac{j_4(x)}{2F} \tag{6}$$

$$\text{species } CO_2: \quad \frac{dN_5}{dx} = \frac{j_4(x)}{2F} \tag{7}$$

$$\text{energy}: \quad -k^{\text{eff}}\frac{d^2T}{dx^2} + \left(\sum_{i=1,3-5} N_i c_{p,i} W_i\right)\frac{dT}{dx} + \left|\frac{j_1(x)+j_4(x)}{2F}\right|(T\Delta S) = (j_1(x)+j_4(x))(\Phi_s - \Phi_m) + \frac{i_m^2}{\kappa^{\text{eff}}} \tag{8}$$

where the reaction rates, $j_1(x)$ and $j_4(x)$ for H_2 and CO, respectively, may be given by the Butler–Volmer equation as

$$j_1(x) = ai_0^{\text{ref}}\theta_1\frac{c_1}{c_1^{\text{ref}}}\left[\exp\left(\frac{\alpha_a F}{RT}(\Phi_s - \Phi_m)\right) - \exp\left(\frac{-\alpha_c F}{RT}(\Phi_s - \Phi_m)\right)\right] \tag{9}$$

$$j_4(x) = ai_0^{\text{ref}}\theta_4\frac{c_4}{c_4^{\text{ref}}}\left[\exp\left(\frac{\alpha_a F}{RT}(\Phi_s - \Phi_m)\right) - \exp\left(\frac{-\alpha_c F}{RT}(\Phi_s - \Phi_m)\right)\right] \tag{10}$$

The parameter i_m is the catalyst layer membrane phase current density, which is related to the proton molar flux, N_2, via the Faraday constant, F, as $i_m = FN_2$. In the energy equation, Eq. (8), ΔS is the entropy change for the cathode reaction, Φ_s and Φ_m are the electrical potential in the catalyst solid phase and catalyst membrane phase, respectively, and κ^{eff} is the effective electrical conductivity of the membrane. The reaction rates $j_1(x)$ and $j_4(x)$, depend on the catalyst reactive surface area per unit volume, a, the reference exchange current density, i_0^{ref}, at the reference oxygen concentration, c_1^{ref}, the fuel concentrations, c_1 and c_4, and the transfer coefficients α_a and α_c. Depending on the characteristics of the half-cell reactions and the material properties of the catalyst layers, the transfer coefficients, α_a and α_c, take on distinct values, each in a range between 0 and 2. In Rowe and Li [13], both transfer coefficients are taken to be unity, which yields an approximate Tafel slope of 70 mV decade^{-1}. In this study, the parameters, α_a and α_c, are considered to be uncertain with the mean value of unity, which reflects both empirical inaccuracy of the parameters in the Butler–Volmer expressions and the run-to-run variations in the operation of the fuel cell.

Since both CO and H_2 are oxidized to produce H^+ [22,31], the species equation for proton flux, Eq. (4), includes the sum of $j_1(x)$ and $j_4(x)$. The species consumption/generation in the electrochemical reaction of carbon monoxide is represented by Eqs. (5)–(7). In the energy equation, Eq. (8), the summation includes four non-ionic species, and the sum $j_1(x)+j_4(x)$ is also introduced for the overall anode electrochemical reaction involving H_2 and CO. Note that the reaction rate $j_1(x)$ is proportional to the coverage of hydrogen molecules, θ_1, which is defined as the fraction of the catalyst reactive surface area covered by the adsorbed hydrogen. Similarly, the reaction rate of the CO species, $j_4(x)$, is considered to be proportional to the CO coverage, θ_4, and CO concentration c_4 in Eq. (10). Considering the adsorption, desorption, and reaction processes of the H_2 and CO species, the coverage θ_1 and θ_4 may be obtained from a kinetic analysis for mass balance [31].

The six conservation equations for the anode catalyst layer, Eqs. (3)–(8) introduce four additional unknowns, namely, c_1, c_4, Φ_s, and Φ_m, which, in turn, are determined by the Nernst–Planck equation and Ohm's law [13]. Note that 10 unknowns are involved in the anode catalyst region: N_1, i_m, N_3, N_4, N_5, T, c_1, c_4, Φ_m, and Φ_s. The governing equations for the cathode catalyst layer follow those given by Rowe and Li [13], and are not repeated here for brevity.

2.3. Membrane

The membrane of a PEM fuel cell is generally made of a perfluorosulfonate polymer, which acts as a proton conductor when saturated with water. Based on the model assumptions, only two species are present in the membrane region, i.e., the liquid water and the proton. Since no chemical reaction takes place in the membrane, the species conservation indicates constant fluxes for both species. The flux of water is determined by the net effect of electro-osmotic drag, diffusion due to concentration gradient, and convection due to pressure gradient. The flux of protons is described by the Nernst–Planck equation, which is further rearranged to be in the form of the membrane potential in this study. The conservation equations of energy and species in the membrane region read [13]:

$$\text{energy}: \quad -k^{\text{eff}}\frac{d^2T}{dx^2} + \frac{d}{dx}(N_l h_l W_l) = \frac{i_m^2}{\kappa} \tag{11}$$

$$\text{potential}: \quad \frac{d\Phi_m}{dx} = -\frac{i_m}{\kappa} + \delta\frac{RT}{F}\left(\frac{3}{1+\delta\lambda}\right)\frac{d\lambda}{dx} + \frac{F}{\kappa}\left(\frac{1}{\lambda}\right)N_l \tag{12}$$

$$H_2O \text{ flux}: \quad N_l = -D_l\frac{dc_l}{dx} - \epsilon_w^{\text{mem}}c_l\frac{k_p}{\mu_v}\left(\frac{dp}{dx}\right) + \frac{\eta_d I}{F} \tag{13}$$

where the subscript 'l' denotes the liquid water species, h the specific enthalpy, κ the proton conductivity of the membrane, δ

the membrane expansion coefficient, λ the membrane hydration, D_l the diffusion coefficient for liquid water in the membrane, ϵ_w^{mem}, the volume fraction of water in the membrane, k_p the hydraulic permeability of the membrane, μ_v the viscosity of liquid water, and η_d is the electro-osmotic drag coefficient. Eqs. (11)–(13) are solved for the three unknowns: T, Φ_m, and N_l, and the readers are referred to Rowe and Li [13] for the values of the various physical properties involved.

The governing equations formulated in Sections 2.1–2.3 are solved with the boundary conditions that the temperature, composition of the reactant gas mixtures, pressure, and flow rate in terms of stoichiometry are specified at the inlets of the anode and cathode electrodes (i.e., at the points a and f in Fig. 1). It must be pointed out that the water vapor flux, N_3, could be calculated by considering the condensation/vaporization processes in the porous electrode regions. However, due to the difficulty in solving two-phase flow in the porous media, the values of N_3 at the electrode/catalyst interfaces, i.e., points b and e, are set to be 10% of the corresponding flux of the reactant mixture, as suggested by Rowe and Li [13] for convenience. An algorithm developed by Fan and White [32] was implemented to predict the polarization curve, temperature distribution, species concentration and flux under various operating conditions. The physical properties and kinetic data adopted in the simulations are available in Refs. [13,31]. The polarization curve can be constructed by solving the governing system of equations for the cell potential, Φ, for different values of the current density, I. The power density of the fuel cell can, in turn, be obtained from the polarization curve as the product of the cell voltage and the corresponding current density.

The deterministic model forms the basis of the stochastic modeling framework discussed in the next section.

3. Stochastic analysis of PEM fuel cells

Stochastic analysis refers to numerical simulation based on a physical model where some of the parameters are uncertain. The approach is that of quantifying the uncertainty in the parameters, propagating the uncertainty through a deterministic model, and analyzing the resulting output parameter distributions for robustness and reliability measures. In the case where the uncertainty in the input parameters can be represented as probability distributions, a sampling method can be used generate stochastic instances (samples) of the uncertain parameters. Through deterministic simulations for each sample, output parameter distributions can be constructed for analysis.

Fig. 2 illustrates the application of the sampling-based stochastic analysis to a polymer electrolyte membrane fuel cell. Several parameters in a fuel cell exhibit varying levels of uncertainty including material parameters such as permeability, porosity of gas diffusion layers, transport properties (such as conductivity, diffusivity), and catalyst loading, among others; model uncertainty associated with phenomenological descriptions, for example, the parameters of the Butler–Volmer equations and operational parameters. The present analysis focuses on modeling uncertainty, in terms of the transfer coefficients, α_a and α_c, of the Butler–Volmer equation, as well as uncertainty in the operating parameters: cell temperature, T; anode and cathode pressures, p_a and p_c; anode and cathode relative humidity, RH_a and RH_c; anode and cathode stoichiometry, ζ_a and ζ_c; dry gas mole fractions at the cathode and anode, x_{N_2/O_2} and x_{CO_2/H_2}, respectively, for a total of 11 uncertain parameters. Other types of uncertainty can also be included following the methodology described here.

The uncertainty in each of the operating parameters is described by a probability distribution function, and quantified

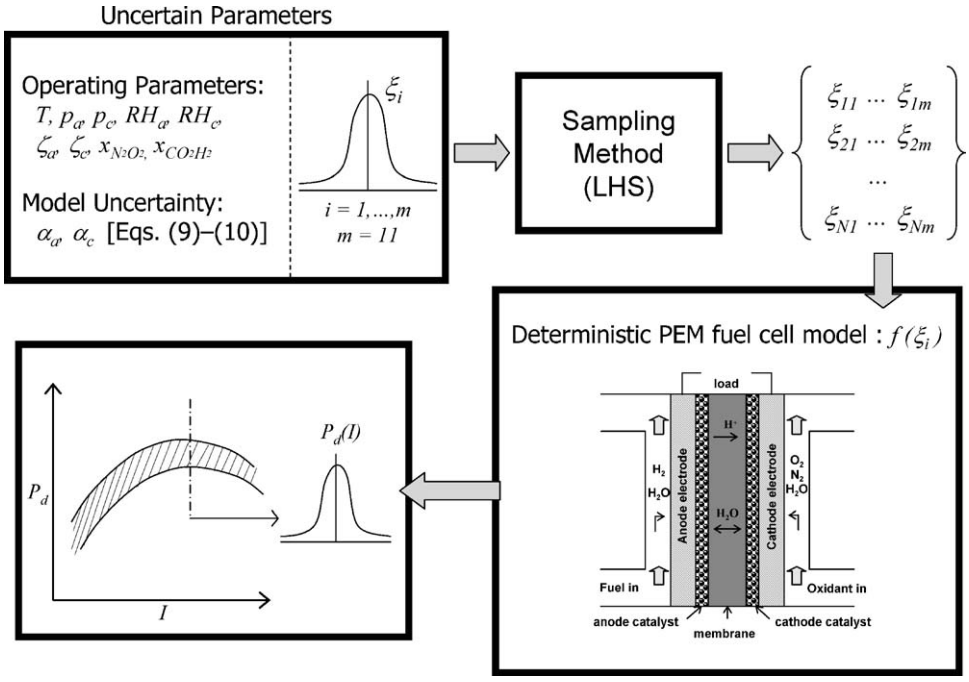

Fig. 2. Schematic diagram of a sampling-based stochastic analysis.

by the distribution's mean value (μ), which denotes the nominal value of the uncertain parameter, and its standard deviation (σ), which is proportional to the uncertainty in the parameter. A degree of uncertainty can be expressed in terms of the coefficient of variance (COV), defined as σ/μ; thus, a deterministic parameter with no uncertainty corresponds to a COV of zero, while a distribution with a large uncertainty has a high coefficient of variance. The choice of the probability density function for each parameter depends on the nature of its uncertainty, and could be one of normal, lognormal, triangular, uniform, Weibull, or other forms as appropriate. Experimental characterization of uncertainty is needed to appropriately define the distribution function. In the absence of such detailed characterization, a normal or Gaussian distribution, which is commonly used to represent uncertain parameters of a physical system, is considered to characterize the uncertain fuel cell model and operating parameters, collectively denoted as ξ_i, $i = 1,\ldots,m$, in Fig. 2.

The combinations of input parameters are selected from their respective distributions using an appropriate sampling technique. The sampling technique and the number of samples are critical for the effectiveness of stochastic model to accurately represent the output distributions corresponding to uncertainty in the input parameters. Theoretically, an infinite number, and practically, a very large number of samples is required to accurately represent an exact continuous probability distribution. In turn, the number of deterministic simulations to be performed in a single stochastic simulation is equal to the required number of samples. Since a single numerical simulation of a PEM fuel cell is computationally expensive, the computational burden of a stochastic simulation, which calls for multiple deterministic simulations, is considerably larger. From a computational viewpoint, therefore, it is desirable to minimize the number of samples in a stochastic simulation.

One approach to alleviating the computational burden is to make the sampling more effective, thus reducing the required number of samples for the stochastic analysis. Stratified sampling methods such as latin hypercube sampling (LHS) [33] offer this advantage over Monte Carlo techniques that are based on truly random sampling. In a stratified sampling method, if N number of samples is required from a one-dimensional distribution, the distribution is divided into N intervals (strata) of equal probability, and one sample is picked randomly from each interval to generate the samples. LHS-generated samples better represent the entire distribution compared to the Monte Carlo technique in which the samples are selected randomly and may not cover the entire distribution. Note that other stratified sampling methods such as the Hammersley sequence sampling [34] may also be used following the methodology presented in this paper.

The LHS method is used to generate a set of N samples from the distributions of the m uncertain parameters, as depicted in Fig. 2. The selection of the number of samples for this study is based on a stochastic convergence analysis discussed in the next section on presentation of results. As noted earlier, the stochastic analysis presented here considers 11 uncertain parameters, i.e., $m = 11$. Each sample, j, represents a combination of the uncertain input parameter values $\{\xi_{ji}: i = 1,\ldots,m\}$, and the deterministic PEM fuel cell model is used to simulate the performance for each such sample, $j = 1,\ldots,N$. The cell polarization curve expressed as the power density variation with the current density, $P_d(I)$, as obtained from the simulations is used as the output parameter for the stochastic analysis.

Based on the multiple simulations corresponding to the N samples, a distribution of the power density variation is obtained as illustrated by the shaded band in Fig. 2. At any given current density, a probability distribution function can be constructed for the power density, which is used to extract the mean (μ_{P_d}), the standard deviation (σ_{P_d}), and the coefficient of variance $[(\sigma/\mu)_{P_d}]$. The results of the stochastic analysis are presented in terms of these parameters in the next section.

4. Results and discussion

Since the PEM fuel cell model described in Section 2 forms the basis of the stochastic analysis, the model is validated first through comparison with numerical and experimental data in the literature. The results of the validation on the polarization curve are presented in Fig. 3, in which the solid lines correspond to the present simulation results, the discrete diamond markers denote numerical prediction by Rowe and Li [13], and the circles represent the experimental data from Springer et al. [10]. The cell potential decreases monotonically with increasing current density, as expected, due to increased ohmic loss in the membrane. The present model predictions show good agreement with the numerical prediction by Rowe and Li [13] over the entire range of current density in the plot.

The model is also validated with the experimental data from Springer et al. [10] where carbon monoxide (CO) poisoning at 100 ppm in the feed hydrogen stream at the anode was considered. The cell potential decreases sharply in the presence of CO poisoning in the anode feed stream, due to the adsorption of CO species on the catalyst surface, which impedes the electrochemical reaction of the hydrogen fuel. Consequently, a smaller cell potential is seen for a fixed value of current density. It should be noted that a sharp drop of cell potential Φ is

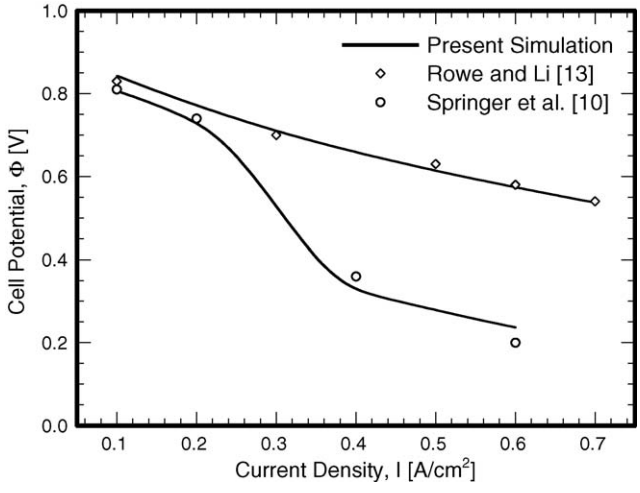

Fig. 3. Validation of the numerical PEM fuel cell model with the data from Refs. [13,10].

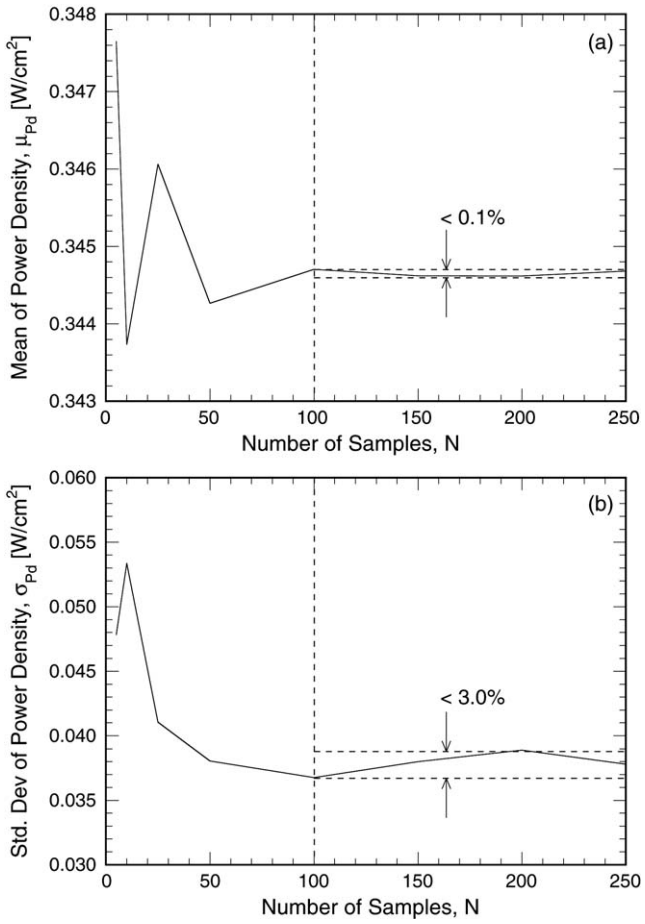

Fig. 4. Stochastic convergence analysis to determine the minimum number of samples: (a) convergence of mean power density with the number of samples and (b) convergence of standard deviation of the power density with the number of samples.

observed between $I = 0.2$ and 0.4 A cm^{-2} for the case with CO poisoning. As current density increases, the loss due to the limitation of mass transport rate becomes dominant, and with further increase in the current density, the partial pressure of oxygen at the catalyst layer/cathode interface rapidly decreases, preventing oxygen from reaching the reaction site and thus rapidly reducing the voltage. The present model predictions are seen to be in close agreement with the experimental data for all current density values. The comparisons in Fig. 3, therefore, demonstrate the accuracy of the deterministic process model, which serves as the basis of the sampling-based stochastic analysis results discussed in the remainder of this section.

The fidelity of the stochastic analysis is directly linked to the accuracy of the shape and moments of the power density distribution obtained from the simulations. While, theoretically, an infinite number of samples is needed for an accurate calculation of the moments, faster computation calls for minimizing the number of samples. The minimum number of samples for the stochastic simulations was determined using a stochastic convergence analysis of the power density distribution. Fig. 4 presents the variations of the mean (Fig. 4(a)) and the standard deviation (Fig. 4(b)) of the power density as a function of the number of samples used in the stochastic simulation. The results correspond to a specific current density of 0.7 A cm^{-2}, and the other operating parameters listed in Table 1. It is observed that both the mean and the standard deviation values converge as the number of samples increases, and, further, that at 100 samples, the mean value converges to within 0.1% (Fig. 4(a)) and the standard deviation value converges to within 3.0% (Fig. 4(b)) of their respective values at larger number of samples. It was found that the convergence characteristic – i.e., the number of samples beyond which the standard deviation (mean) converges to within 3.0% (0.1%) – remained practically invariant to the change in the initial random seed used in the generation of the samples using LHS. Based on the stochastic convergence analysis, a sample size of 100 was selected for the simulations reported in this section.

Table 1
Values of the operating parameters used in the studies

Operating parameters	Figs. 4–6	Figs. 7–12
Current density, I (A cm^{-2})	0.7	Variable
Cell temperature, T (°C)	100	100
Anode pressure, p_a (atm)	6.5	10
Cathode pressure, p_c (atm)	6.5	15
Anode stoichiometry, ζ_a	4.0	1.1
Cathode stoichiometry, ζ_c	4.0	7.0
Anode relative humidity, RH_a	0.6	1.1
Cathode relative humidity, RH_c	0.6	0.1
Anode dry gas mole fraction, x_{CO_2/H_2}	0.0	0.0
Cathode dry gas mole fraction, x_{N_2/O_2}	3.76	0.0

Fig. 5 shows a distribution of the power density from a stochastic simulation corresponding to a current density of 0.7 A cm^{-2}. Recall that the uncertain parameters in the stochastic simulations are represented as symmetric Gaussian distributions; however, the histogram of the power density reveals a distinct skew in the distribution, which reflects the nonlinearity of the relationship between the power density and the uncertain parameters. Furthermore, it is important to note that as a result of the nonlinearities, the extreme values of the power

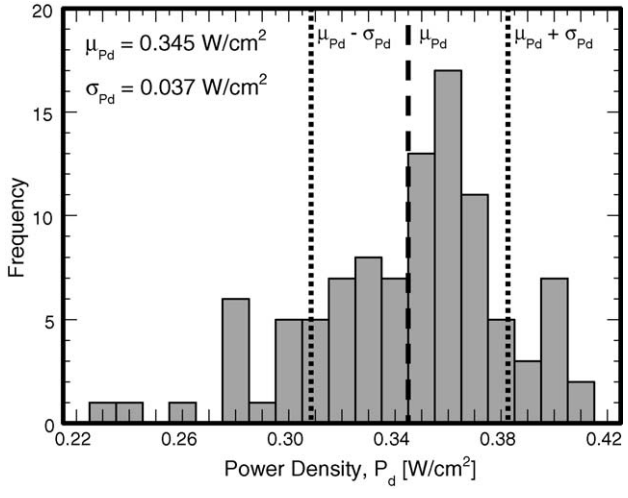

Fig. 5. Power density distribution obtained from stochastic analysis using 100 samples.

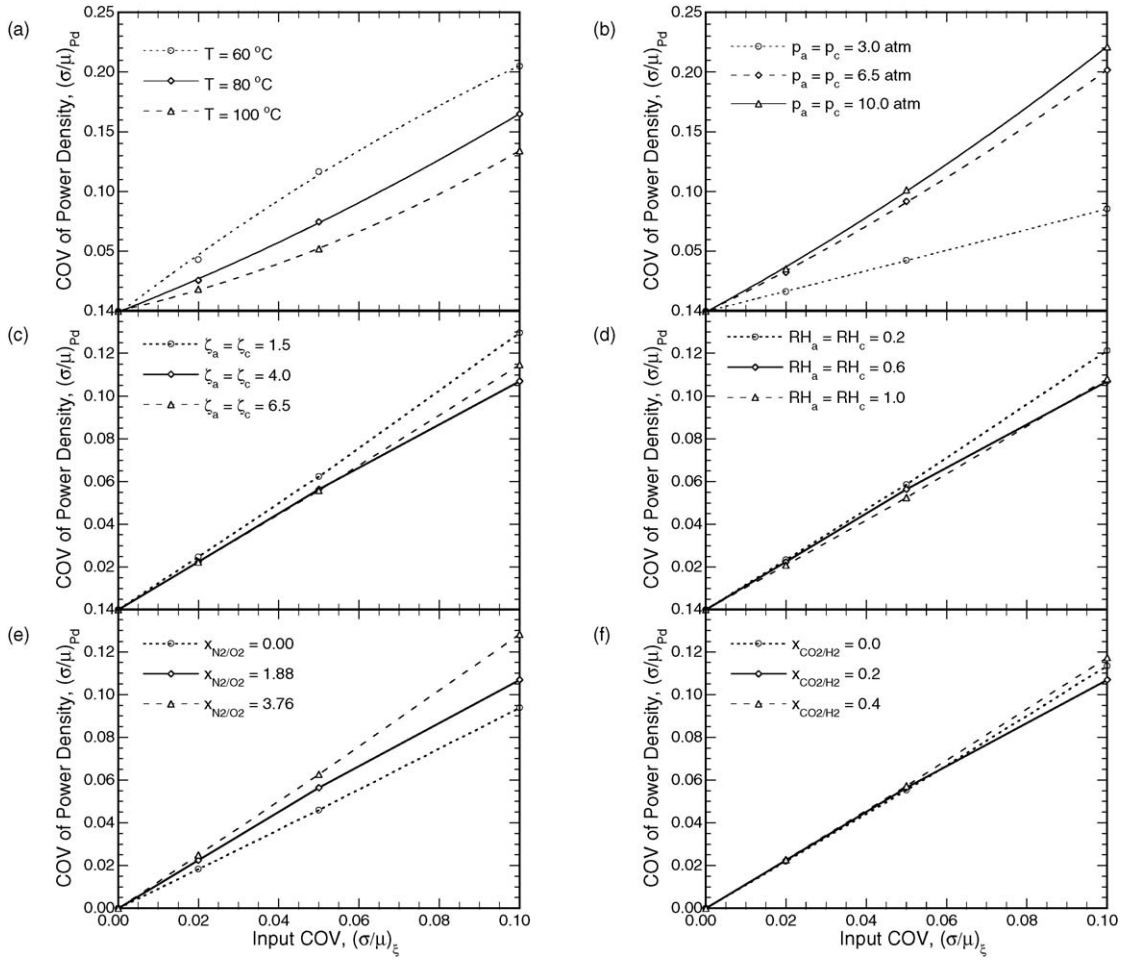

Fig. 6. Coefficient of variance of power density as a function of input uncertainty for various values operating parameters: (a) cell temperature, (b) anode and cathode pressures, (c) anode and cathode stoichiometry, (d) relative humidity in the anode and cathode, (e) N_2/O_2 mole fraction, and (f) CO_2/H_2 mole fraction.

density do not necessarily correspond to the extreme values of the uncertain input parameter distributions; thus, a sampling-based stochastic analysis is better suited for robust design than other techniques such as interval analysis that consider only the extreme values of the uncertain parameter ranges. The bold-dashed-line in Fig. 5 represents the mean value of the distribution ($\mu_{P_d} = 0.345\,\mathrm{W\,cm^{-2}}$) and the dotted lines at 0.308 and $0.382\,\mathrm{W\,cm^{-2}}$ indicate $\mu_{P_d} - \sigma_{P_d}$ and $\mu_{P_d} + \sigma_{P_d}$ values, respectively. It is seen that about 75% of the distribution falls within this one-standard deviation band around the mean. The figure suggests that the mean, μ_{P_d}, the standard deviation, σ_{P_d}, and the coefficient of variance, $(\sigma/\mu)_{P_d}$, are appropriate measures of the power density distribution and will be used in the analysis presented here.

Fig. 6 shows the coefficient of variance (COV) of the power density as a function of input uncertainty, expressed as the COV of the input parameters, $(\sigma/\mu)_\xi$, for various values of the operating parameters under uncertainty. It should be noted that as each operating parameter shown in Fig. 6 is varied, the other parameters assume the values listed in Table 1. The results share a common trend that as the COV of the input parameters increases, the COV of power density also increases. Fig. 6(a) presents the effects of the cell temperature, T, in which it is seen that higher cell temperature results in lower COV of the power density for all values of input COV, $(\sigma/\mu)_\xi$. It was reported in Ref. [22] that power density increases with increasing cell temperature. Thus the results indicate that as the cell temperature increases, the increase in the standard deviation of power density is less than the increase in the mean power density, causing the COV of power density, $(\sigma/\mu)_{P_d}$, to decrease as T increases. The effects of varying electrode pressures, p_a and p_c, on the COV of power density are presented in Fig. 6(b), which shows that lower electrode pressures cause smaller power density variance. However, it should be noted that small values of electrode pressures also result in small power density [22], which may not be a desirable performance. Fig. 6(c)–(f) show that the effects of the variation in the anode and cathode stoichiometry, ζ_a and ζ_c, relative humidity of the anode and cathode, RH_a and RH_c, and dry gas mole fractions, x_{N_2/O_2} and x_{CO_2/H_2}, on the power density variance are less significant than the effects of T, p_a and p_c, for all values of $(\sigma/\mu)_\xi$. For the remainder of the parametric study of the stochastic analysis, therefore, the paper focuses on the effects of operating cell temperature, T, anode pressure, p_a, and cathode pressure, p_c, on the variation of power density.

Fig. 7(a)–(i) present the mean power density, μ_{P_d}, as a function of the current density for a range of input parameter uncer-

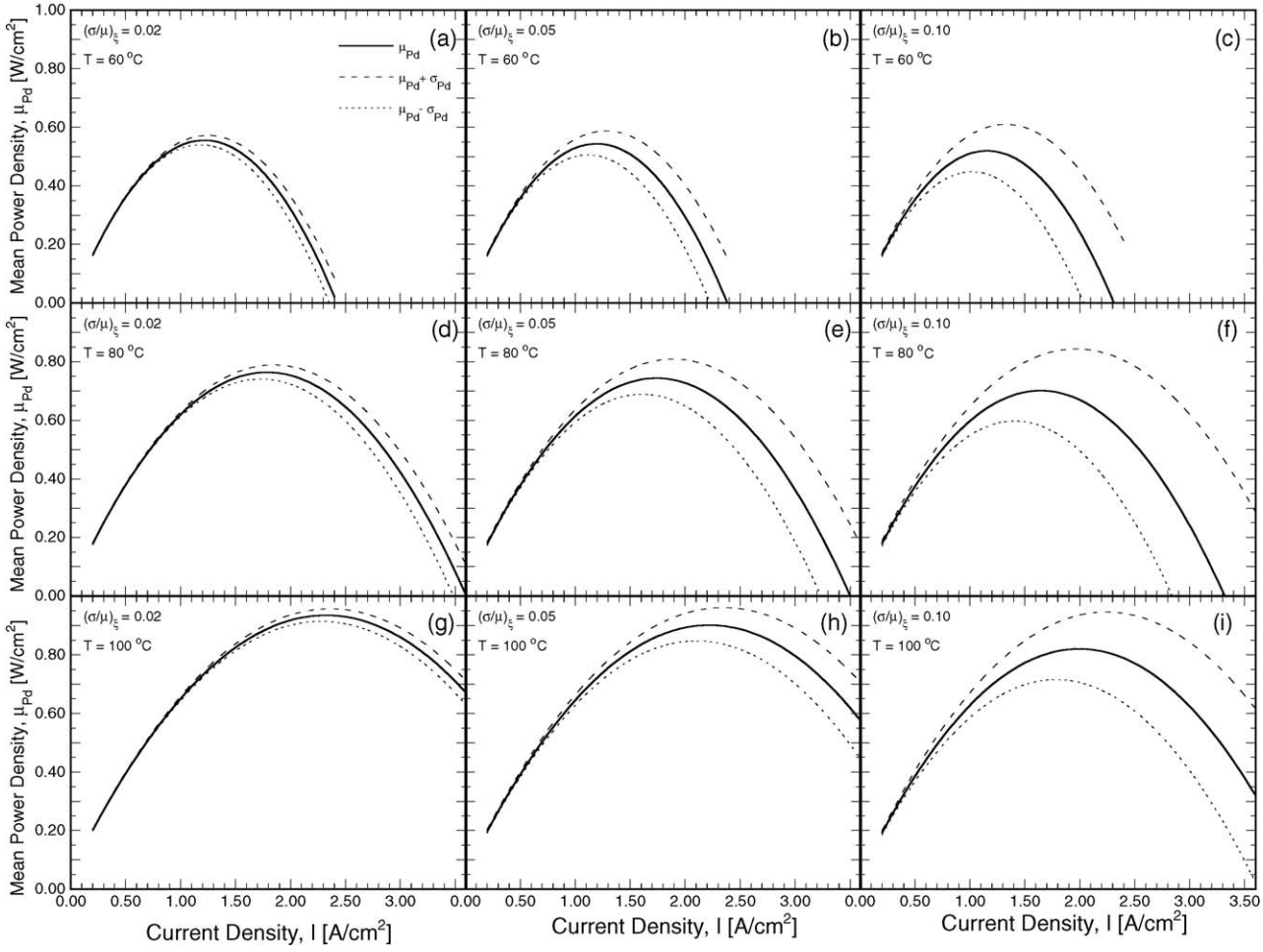

Fig. 7. Mean and standard deviation values of power density as a function of current density at various values of cell temperature and level of input uncertainty. Other operating parameters are given in Table 1.

tainty, $(\sigma/\mu)_\xi$ and cell temperature, T. The variability in the power density as a function of the current density is illustrated by the dashed lines, which represent the values of $\mu_{P_d} - \sigma_{P_d}$ and $\mu_{P_d} + \sigma_{P_d}$. For a given current density, the standard deviation of the power density, σ_{P_d}, is the magnitude of the difference between either of the two dashed lines and the solid line in the plots. The results show that as the current density increases, the variability of power density also increases as seen in the widening of the gap between the dashed lines in the plot. The increase is more pronounced for cases with higher input uncertainty, as observed in Fig. 7(c), (f), and (i) (the right column of plots). As $(\sigma/\mu)_\xi$ increases (from left to right in Fig. 7), the peak mean power density slightly decreases, while the standard deviation of the power density, σ_{P_d}, clearly increases, which signifies that increase in the input parameter uncertainty leads to a significant performance variability of the fuel cell. As the cell temperature increases (from top to bottom in Fig. 7), both the mean and the standard deviation of the power density increase. However, the increase in the mean value dominates the increase in the standard deviation, resulting in a decrease in the coefficient of variance, $(\sigma/\mu)_{P_d}$, with temperature, T, as noted in Fig. 6(a). These results suggest that the fuel cell should be operated at high temperature from the viewpoint of increasing the mean power density, μ_{P_d}; however, minimizing variance, σ_{P_d}, calls for a low temperature operation. Identification of robust operating regimes is based on balancing these two competing considerations.

It is instructive to examine the variation of the mean values of the power density with respect to their corresponding standard deviations so that the maximum achievable mean power density can be identified for an allowable maximum variance in the power density. To this end, Fig. 8(a)–(c) present the data from Fig. 7 in this format, for σ_{P_d} in the range of 0–0.10 W cm^{-2}, and for the three input uncertainty levels and the three temperatures considered in Fig. 7. For a given value of σ_{P_d}, the mean power density, μ_{P_d}, increases with cell temperature, owing to the reduced activation and concentration losses, and decreases as $(\sigma/\mu)_\xi$, increases (Fig. 8(a)–(c)). It is seen in Fig. 8(a)–(c) that for each combination of temperature and input uncertainty, the mean power density is maximized, $\mu^*_{P_d}$, for an optimum value of the standard deviation, $\sigma^*_{P_d}$, as identified for an example case in Fig. 8(a). This suggests that in order to operate the fuel cell at its maximum power density, a certain degree of variability represented by $\sigma^*_{P_d}$ is inevitable, and that the variability can not be reduced (or increased) further without also compromising on the mean power density. It is interesting to note that the mean power density is reduced for both a tighter and a relaxed specification on

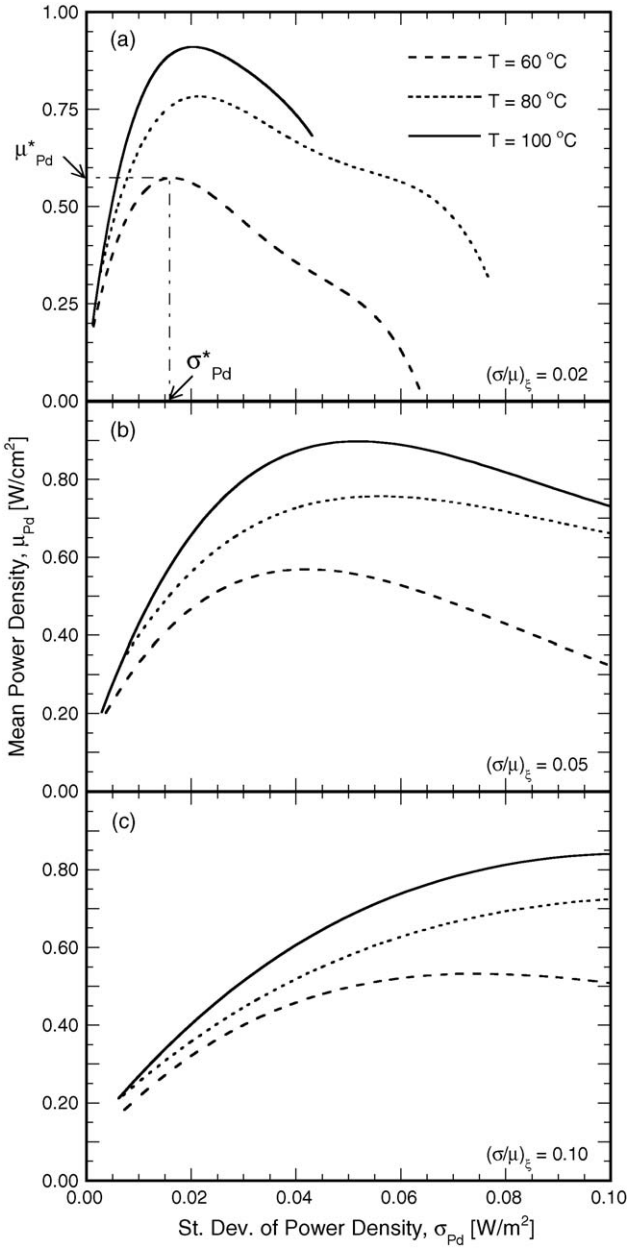

Fig. 8. Mean value of power density as a function of the standard deviation for various values of cell temperature and level of input uncertainty. Other operating parameters are given in Table 1.

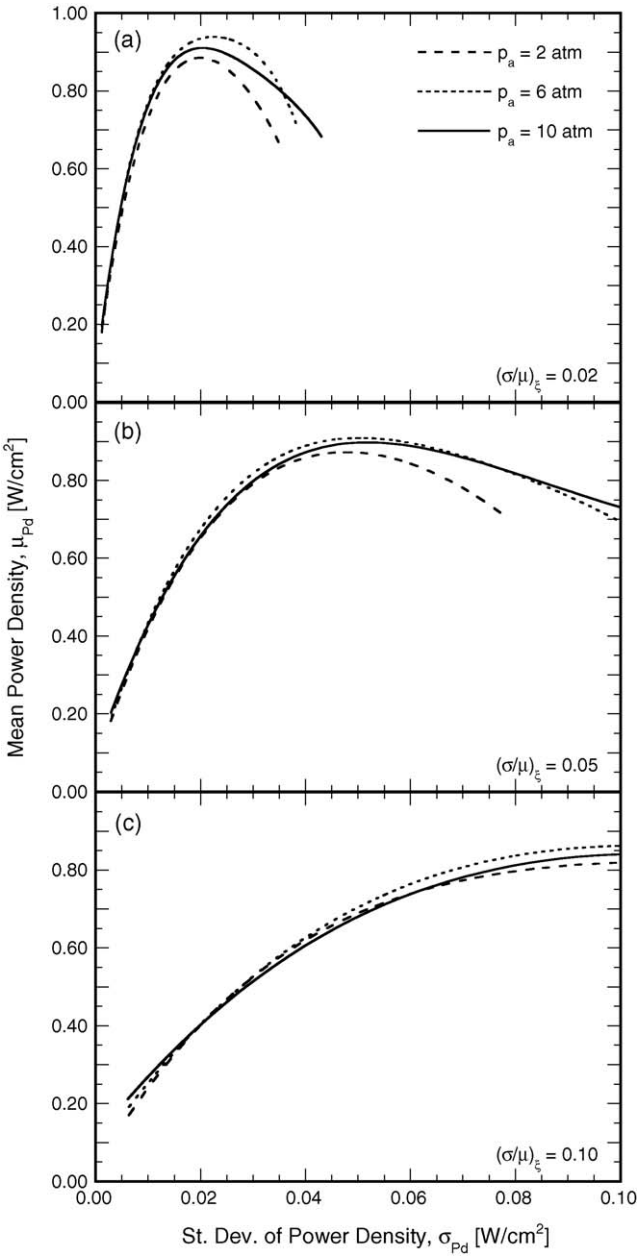

Fig. 9. Mean value of power density as a function of the standard deviation for various values of anode pressure and level of input uncertainty. Other operating parameters are given in Table 1.

the allowable variance relative to $\sigma^*_{P_d}$. Fig. 8 further shows that the optimum variance increases with temperature at all levels of input uncertainty. For a given temperature, $\sigma^*_{P_d}$, increases with $(\sigma/\mu)_\xi$, which indicates that as the input uncertainty increases, the fuel cell can not be operated at the maximum power density without corresponding increase in the variability.

Following the format in Fig. 8, Fig. 9 illustrates the effects of anode pressure, p_a on the mean and standard deviation of power density, at a cell temperature of $T = 100\,^\circ$C and cathode pressure of $p_c = 15$ atm. It is also observed that for each anode pressure, there exists an optimum standard deviation of power density, $\sigma^*_{P_d}$, which corresponds to a peak value of mean power density, $\mu^*_{P_d}$. As input COV, $(\sigma/\mu)_\xi$, increases (Fig. 9(a)–(c)), $\sigma^*_{P_d}$, increases, and the corresponding peak mean power density, $\mu^*_{P_d}$, decreases, for all values of anode pressure considered. Both peak mean power density, $\mu^*_{P_d}$, and the optimum standard deviation, $\sigma^*_{P_d}$, exhibit a non-monotonic trend with respect to the anode pressure, with $p_a = 6$ atm being an optimum within the range of anode pressures considered. At the low anode pressures, an increase in p_a enhances the power density due to reduced concentration loss. However, further increase in p_a causes membrane dehydration and lower performance due to a decrease in the water diffusivity in the anode region [23]. It should also be noted that the effects of anode pressure on the variation of power density are not as significant as those of the cell temperature seen in Fig. 8.

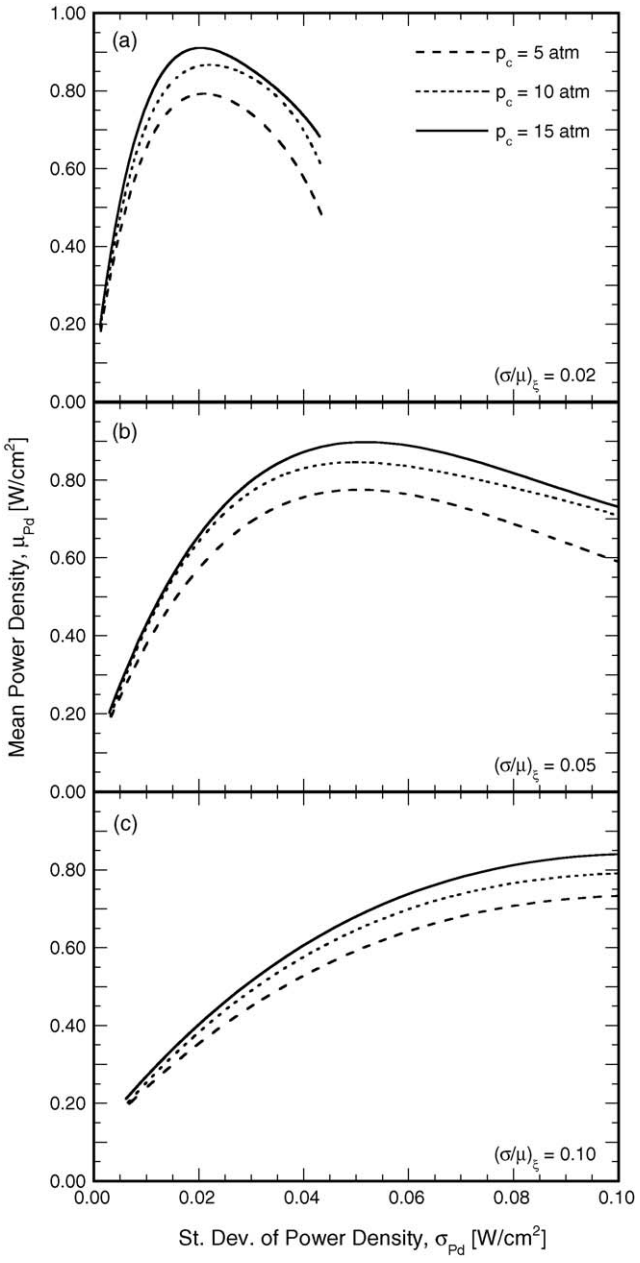

Fig. 10. Mean value of power density as a function of the standard deviation for various values of cathode pressure and level of input uncertainty. Other operating parameters are given in Table 1.

The effects of cathode pressure on the mean power density variation with the standard deviation are shown in Fig. 10, for input COV of 0.02 (Fig. 10(a)), 0.05 (Fig. 10(b)), and 0.10 (Fig. 10(c)), with the cell temperature fixed at $T = 100\,^{\circ}\mathrm{C}$ and anode pressure at $p_c = 10$ atm. It is observed that as the cathode pressure, p_c, increases, the mean power density, μ_{P_d}, increases monotonically, for any value of the standard deviation, due to the reduced concentration loss at the high cathode pressure. Further, as previously observed in Figs. 8 and 9, the optimum standard deviation of power density, $\sigma^*_{P_d}$, also increases as the $(\sigma/\mu)_\xi$ increases. For the values of cell temperature, cathode pressure, and input COV considered, both the peak mean power density, $\mu^*_{P_d}$, and the optimum standard deviation, $\sigma^*_{P_d}$, increase monotonically with p_c. The results in Fig. 10 also indicate that the effects of the cathode pressure, p_c, are more significant than those of the anode pressure.

From the foregoing results, it is evident that conditions that lead to maximizing the mean power density also cause the variability to increase. Thus, it is of interest to determine the optimum cell temperature, and anode and cathode pressures, which maximize the mean power density subject to constraint on limiting the standard deviation of power density to within a desired value, for given input uncertainty. The results in Figs. 8–10 can be used to construct design charts that provide for determining the maximum achievable mean power density as a function of input COV and desired maximum standard deviation of power density. The design charts and the illustration of the design methodology are the focus of the remainder of the discussion.

Fig. 11 presents contour maps of the maximum realizable mean power density, $\mu_{P_{d,max}}$, as a function of the standard deviation, σ_{P_d}, and input coefficient of variance, $(\sigma/\mu)_\xi$, for the three values of the cell temperature. For all the three cell temperatures, the contours exhibit similar trends with different magnitude of power density values. The maximum realizable mean power density varies from $0.56\,\mathrm{W\,cm^{-2}}$ for $T = 60\,^{\circ}\mathrm{C}$ (Fig. 11(a)) to $0.93\,\mathrm{W\,cm^{-2}}$ (Fig. 11(c)). The maximum power density values are seen to concentrate along a band extending from the lower left corner to the top mid section of each plot frame. The design plots reveal interesting trends: for stringent requirements on the maximum variability, for example $\sigma_{P_d} = 0.02\,\mathrm{W\,cm^{-2}}$, the maximum achievable mean power density decreases monotonically as $(\sigma/\mu)_\xi$ increases. However, if a greater variability were tolerable, for example, $(\sigma/\mu)_\xi = 0.05\,\mathrm{W\,cm^{-2}}$, $\mu_{P_{d,max}}$, increases for $0 \le (\sigma/\mu)_\xi < 0.05$ and decreases for $(\sigma/\mu)_\xi > 0.05$.

The contours of maximum mean power density corresponding to different anode and cathode pressures are presented in Fig. 12(a)–(c) and (d)–(f), respectively, for a fixed cell temperature of 100 °C. The shapes of the contours in Fig. 12 are similar in shape to those in Fig. 11, in that the larger values of the mean power density are clustered around regions in each plot. The magnitude of the maximum achievable mean power density, $\mu_{P_{d,max}}$, increases as the anode pressure increases from $p_a = 2$ atm (Fig. 12(a)) to $p_a = 6$ atm (Fig. 12(b)), and slightly decreases with further increase of p_a to 10 atm (Fig. 12(c)). On the other hand, the results for different values of cathode pressure in Fig. 12(d)–(f) show that the maximum mean power density increases monotonically with cathode pressure, reaching a value of $0.93\,\mathrm{W\,cm^{-2}}$ for $p_c = 15$ atm (Fig. 12(f)). Once again, the maximum achievable mean power density is seen to decrease monotonically with $(\sigma/\mu)_\xi$ at small values of allowable, σ_{P_d}, whereas at larger allowable values, a non-monotonic trend is evident in the variation of $\mu_{P_{d,max}}$ with $(\sigma/\mu)_\xi$.

The use of the contour maps in Figs. 11 and 12 for a robust design of the fuel cell operating parameters is illustrated by considering three design cases—Case A in which the variance in power density, σ_{P_d}, is to be limited to $0.02\,\mathrm{W\,cm^{-2}}$ for a cell with an operational parameter uncertainty, $(\sigma/\mu)_\xi = 0.10$; Case B in which the variance in power density, σ_{P_d}, is to be limited to $0.02\,\mathrm{W\,cm^{-2}}$ for a cell with an operational parameter uncertainty, $(\sigma/\mu)_\xi = 0.05$ and Case C in which the variance in power

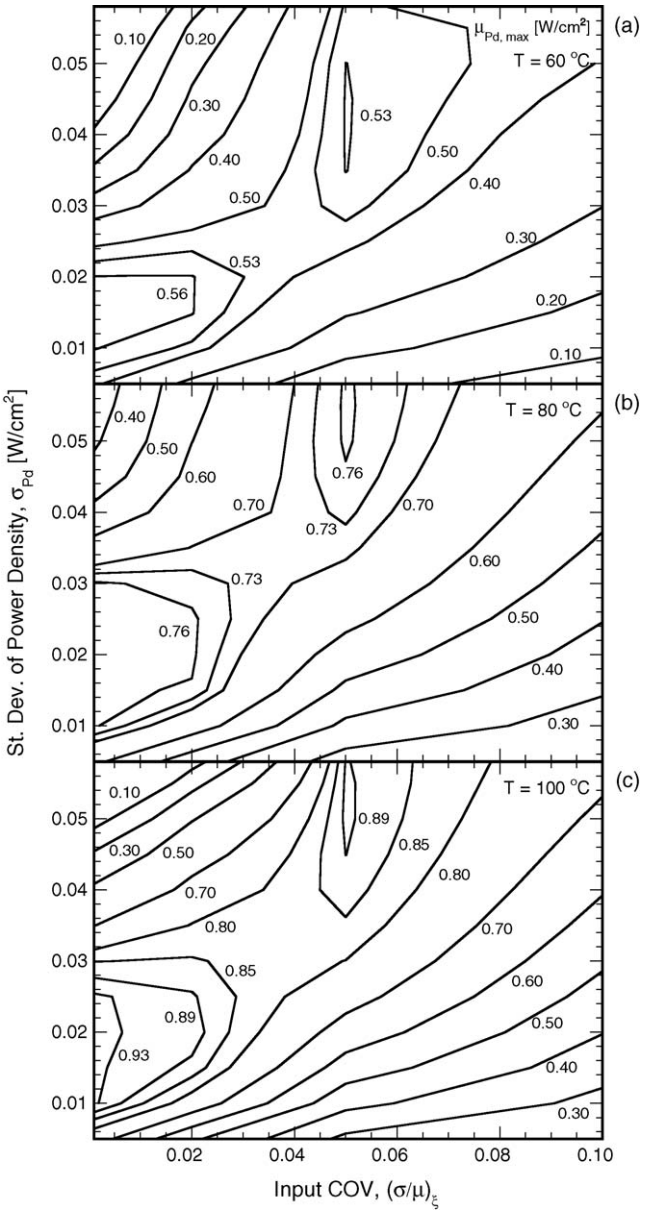

Fig. 11. Contour maps representing the maximum mean value of power density, in a two-dimensional field of the standard deviation of power density and input uncertainty, for various values of cell temperature. Other operating parameters are given in Table 1.

density, σ_{P_d}, is to be limited to 0.05 W cm^{-2} for a cell with an operational parameter uncertainty, $(\sigma/\mu)_\xi = 0.05$.

- Corresponding to Case A specifications, it is seen from Fig. 11 that the maximum realizable mean power density, $\mu_{P_d,\max}$, is highest at 0.40 W cm^{-2} for an operating temperature of 100 °C, and anode and cathode pressures of 10 and 15 atm, respectively (Fig. 11(c)). Similarly, Fig. 12(a)–(c) reveal that the design specifications for Case A correspond to a maximum achievable mean power density of 0.40 W cm^{-2} for all anode pressures in the range 2–10 atm, a cell temperature of 100 °C and a cathode pressure of 15 atm, and Fig. 12(d)–(f) indicate that the maximum realizable mean power density is 0.40 W cm^{-2} for $p_c = 15$ atm, $T = 100$ °C and $p_a = 10$ atm. Based on these, the robust operating conditions for Case A are deduced as $T = 100$ °C, $p_a = 2$ atm, and $p_c = 15$ atm. Note that the solution is invariant to the anode pressure, and the lowest value of 2 atm is chosen based on minimizing the pumping requirements. The robust solution yields a mean power density of 0.40 W cm^{-2} with a variability of 0.02 W cm^{-2}, which represents a coefficient of variance of 5% on the power density.
- Case B denotes a reduction in the parameter uncertainty to 5% while the variability on the power density is sought to be kept within 0.02 W cm^{-2} as in Case A. Corresponding to these specifications, the following parameter combinations and maximum realizable power densities are obtained from Figs. 11 and 12: $T = 100$ °C, $p_a = 10$ atm, $p_c = 15$ atm, $\mu_{P_d,\max} = 0.65$ W cm^{-2} (Fig. 11(c)); $T = 100$ °C, $p_a = 6$ atm, $p_c = 15$ atm, $\mu_{P_d,\max} = 0.68$ W cm^{-2} (Fig. 12(b)) and $T = 100$ °C, $p_a = 10$ atm, $p_c = 15$ atm, $\mu_{P_d,\max} = 0.65$ W cm^{-2} (Fig. 12(c)). The operating parameters that lead to the maximum mean power density of 0.68 W cm^{-2}, noted above from Fig. 12(b), therefore, constitute the robust parameter design for Case B. For this design, and the variability of 0.02 W cm^{-2}, the coefficient of variance on the power density is 2.9%.
- Case C explores the impact of accommodating a greater variability in the power density, while the parameter uncertainty is maintained at 5% as in Case B. The reader may verify that the robust operating conditions that lead to maximum mean power density correspond to the parameter combination in Fig. 12(b), as in Case B: $T = 100$ °C, $p_a = 6$ atm, $p_c = 15$ atm, for which the maximum realizable power density is 0.90 W cm^{-2}, and its coefficient of variance is 5.6%.

A comparison of the three design cases indicates that reducing the parameter uncertainty from 10% (Case A) to 5% (Case B) leads to a 70% increase in the maximum realizable power density from 0.40 to 0.68 W cm^{-2}. Further, by allowing for a greater variability of 0.05 W cm^{-2} in the power density (Case C) while keeping the parameter uncertainty at 5%, the mean power density is increased to 0.90 W cm^{-2}—an increase of 32% relative to the 0.68 W cm^{-2} in Case B. Of the three cases, the design for Case B represents the least coefficient of variance of the power density. The contour maps in Figs. 11 and 12 thus provide for ready exploration of tradeoffs in arriving at robust designs based on application requirements.

The results presented here were based on parametric studies over a selected range of three principal operating parameters in order to illustrate the methodology of fuel cell design under uncertainty using stochastic simulations. The stochastic analysis methodology may be extended to design considerations involving parameters other than the power density, and moreover, other considerations, such as those involved in the application of high cell pressures, may be incorporated as additional objectives and constraints in the design endeavor. The stochastic analysis methodology was demonstrated in this study using a one-dimensional single-phase model of a PEM fuel cell, which served to illustrate the principal trends and results that are appli-

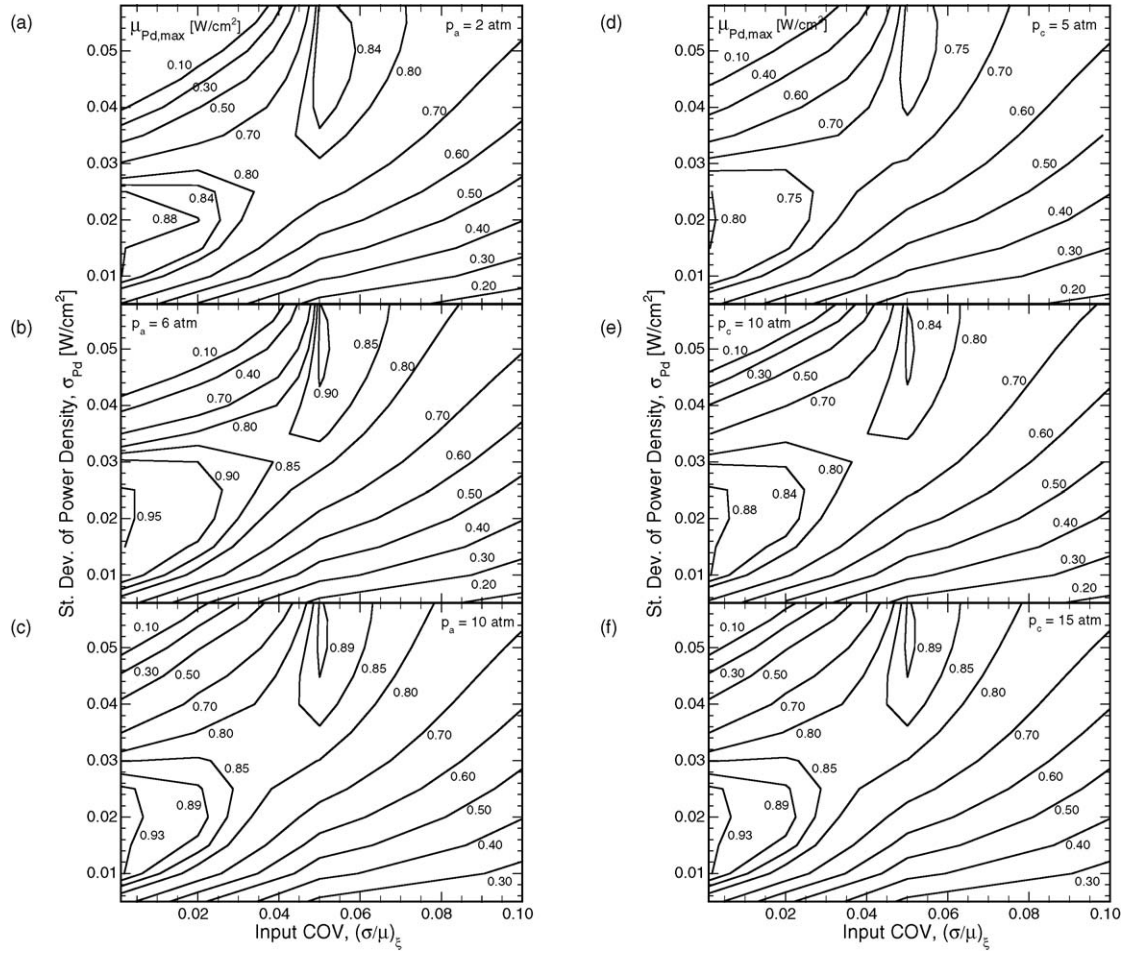

Fig. 12. Contour maps representing the maximum mean value of power density, in a two-dimensional field of the standard deviation of power density and input uncertainty, for: (a)–(c) various values of anode pressure and (d)–(f) various values of cathode pressure. Other operating parameters are given in Table 1.

cable to practical fuel cells. The methodology can be readily extended to more sophisticated multi-dimensional and multi-phase models of fuel cells and their stacks with an associated increase in the computational effort. These enhancements may be considered in a future study. In a future work, the stochastic modeling framework may also be interfaced with a numerical optimization scheme to provide a robust design tool for stochastic optimization under uncertainty.

5. Conclusions

The paper presented detailed discussion on the framework of a sampling-based stochastic analysis for proton exchange membrane fuel cells, where some of the operating and design parameters (input parameters) are uncertain. The results were presented in terms of mean and standard deviation of power density, which represent a performance measure and its variability. The methodology and the results provide for a valuable tool for fuel cell design under uncertainty. Example cases illustrating the use of the results for robust design under uncertainty were presented. The stochastic analysis framework presented in the paper may be used for cases where other input parameters are considered to be uncertain. The stochastic model can also be used as a basis for numerical optimization under uncertainty for fuel cells.

Acknowledgements

The work was funded by the U.S. Army RDECOM through contract no. DAAB07-03-3-K-415. The authors also acknowledge the help of Dr. Yonghong Yan in developing the code used for the simulations reported in this work.

References

[1] J. Larminie, A. Dicks, Fuel Cell Systems Explained, Wiley, West Sussex England, 2000.
[2] C. Marr, X. Li, An engineering model of proton exchange membrane fuel cell performance, ARI 50 (1998) 190–200.
[3] T.V. Nguyen, R.E. White, A water and heat management model for proton exchange membrane fuel cells, J. Electrochem. Soc. 140 (8) (1993) 2178–2186.
[4] T.F. Fuller, J. Newman, Water and thermal management in solid polymer electrolyte fuel cells, J. Electrochem. Soc. 140 (5) (1993) 1218–1225.
[5] D.M. Bernardi, Water-balance calculations for solid polymer electrolyte fuel cells, J. Electrochem. Soc. 137 (11) (1990) 3344–3351.
[6] T.A. Zawodzinski, T.A. Springer, J. Davey, R. Jestel, C. Lopez, J. Valero, S. Gottesfeld, A comparative study of water uptake and transport through

iononomeric fuel cell membranes, J. Electrochem. Soc. 140 (7) (1993) 1981–1985.
[7] T.A. Zawodzinski, C. Derouin, S. Radzinski, R.J. Sherman, V.T. Smith, T.A. Springer, S. Gottesfeld, Water uptake by and transport through Nafion 117 membranes, J. Electrochem. Soc. 140 (4) (1993) 1041–1047.
[8] D.M. Bernardi, M.W. Verbrugge, Mathematical model of a gas diffusion electrode bonded to a polymer electrolyte, AIChE J. 37 (8) (1991) 1151–1163.
[9] D.M. Bernardi, M.W. Verbrugge, A mathematical model of the solid polymer electrolyte fuel cell, J. Electrochem. Soc. 139 (9) (1992) 2477–2745.
[10] T.E. Springer, T.A. Zawodzinski, S. Gottesfeld, Polymer electrolyte fuel cell model, J. Electrochem. Soc. 138 (8) (1991) 2334–2342.
[11] T.E. Springer, M.S. Wilson, S. Gottesfeld, Modeling and experimental diagnostics in polymer electrolyte fuel cells, J. Electrochem. Soc. 140 (12) (1993) 3513–3526.
[12] J.J. Baschuk, X. Li, Modelling of polymer electrolyte membrane fuel cells with variable degrees of water flooding, J. Power Sources 86 (2000) 181–196.
[13] A. Rowe, X. Li, Mathematical modeling of proton exchange membrane fuel cells, J. Power Sources 102 (2001) 82–96.
[14] J.C. Amphlett, R.M. Baumert, R.F. Mann, B.A. Peppley, P.R. Roberge, Performance modeling of the Ballard Mark IV solid polymer electrolyte fuel cell, J. Electrochem. Soc. 142 (1) (1995) 1–15.
[15] J.C. Amphlett, R.F. Mann, B.A. Peppley, P.R. Roberge, A. Rodrigues, A model predicting transient responses of proton exchange membrane fuel cells, J. Power Sources 61 (1996) 183–188.
[16] V. Gurau, H. Liu, S. Kakac, Two-dimensional model for proton exchange membrane fuel cells, AIChE J. 44 (11) (1998) 2410–2422.
[17] S. Um, C.Y. Wang, K.S. Chen, Computational fluid dynamics modeling of proton exchange membrane fuel cells, J. Electrochem. Soc. 147 (2000) 4485–4493.
[18] Z.H. Wang, C.Y. Wang, K.S. Chen, Two-phase flow and transport in the air cathode of proton exchange membrane fuel cells, J. Power Sources 94 (2001) 40–50.
[19] L. You, H. Liu, A two-phase flow and transport model for the cathode of PEM fuel cells, Int. J. Heat Mass Transfer 45 (2002) 2277–2287.
[20] You, L. The two phase flow, transport mechanism and performance studies for PEM fuel cells, PhD Dissertation, University of Miami, 2001.
[21] V. Mishra, F. Yang, R. Pitchumani, Measurement and prediction of electrical contact resistance between gas diffusion layers and bipolar plate for applications to PEM fuel cells, ASME J. Fuel Cell Sci. Technol. 1 (2004) 2–9.
[22] V. Mishra, F. Yang, R. Pitchumani, Analysis and design of PEM fuel cells, J. Power Sources 141 (2005) 47–64.
[23] A. Mawardi, F. Yang, R. Pitchumani, Optimization of the operating parameters of a proton exchange membrane fuel cell for maximum power density, ASME J. Fuel Cell Sci. Technol. 2 (2005) 121–135.
[24] K. Subramanyan, U.M. Diwekar, Characterization and quantification of uncertainty in solid oxide fuel cell hybrid power plants, J. Power Sources 142 (2005) 103–116.
[25] K. Subramanyan, U.M. Diwekar, A. Goyal, Multi-objective optimization for hybrid fuel cells power system under uncertainty, J. Power Sources 132 (2004) 99–112.
[26] S.K. Padmanabhan, R. Pitchumani, Stochastic analysis of isothermal cure of resin systems, Polym. Compos. 20 (1999) 72–85.
[27] A. Mawardi, R. Pitchumani, Cure cycle design for thermosetting-matrix composites fabrication under uncertainty, Ann. Oper. Res. 132 (2004) 19–45.
[28] U. Pasaogullari, C.Y. Wang, Liquid water transport in gas diffusion layer of polymer electrolyte fuel cells, J. Electrochem. Soc. 151 (2004) A399–A406.
[29] U. Pasaogullari, C.Y. Wang, Two-phase transport and the role of microporous layer in polymer electrolyte fuel cells, Electrochim. Acta 49 (2004) 4359–4369.
[30] U. Pasaogullari, C.Y. Wang, K.S. Chen, Two-phase transport in polymer electrolyte fuel cells with bilayer diffusion media, J. Electrochem. Soc. 152 (2005) A1574–A1582.
[31] T.E. Springer, T. Rockward, T.A. Zawodzinski, S. Gottesfeld, Model for polymer electrolyte fuel cell operation on reformate feed, J. Electrochem. Soc. 148 (11) (2001) A11–A23.
[32] D. Fan, R.E. White, Modification of Newman's BAND(J) subroutine to multi-region systems containing interior boundaries: MBAND, J. Electrochem. Soc. 138 (6) (1991) 1688–1691.
[33] R.L. Iman, M.J. Shortencarier, A FORTRAN77 program and user's guide for generation of latin hypercube and random samples for use with computer models, Technical Report, NUREG/CR-3624, SAND83-2365, Sandia National Laboratories, Albuquerque NM, 1984.
[34] J. Kalagnanam, U. Diwekar, An efficient sampling technique for off-line quality control, Technometrics 39 (1997) 308–319.